E-proceedings of the 36th IAHR World Congress
28 June – 3 July, 2015, The Hague, the Netherlands

INTEGRAL TURBULENT LENGTH AND TIME SCALES IN HYDRAULIC JUMPS: AN EXPERIMENTAL INVESTIGATION AT LARGE REYNOLDS NUMBERS

HANG WANG(1) & HUBERT CHANSON(1)

(1) The University of Queensland, School of Civil Engineering, Brisbane QLD 4072, Australia,
hang.wang@uqconnect.edu.au

ABSTRACT

A hydraulic jump is a rapidly-varied open channel flow characterised by the sudden transition from a supercritical flow motion to a subcritical regime. The transition is associated with a rapid increase of water depth, a highly turbulent flow with macro-scale vortices, significant kinetic energy dissipation, a two-phase flow region and some strong turbulence interactions with the free surface leading to splashes and droplet projection. The phenomenon is not a truly random turbulent process because of the existence of low-frequency, pseudo-periodic coherent structures and fluctuating motion in the jump roller. This study presents new measurements of turbulent air-water flow properties in hydraulic jumps, including turbulence intensity, longitudinal and transverse integral length and time scales, for a range of Froude numbers ($3.8 < Fr_1 < 8.5$) at large Reynolds numbers ($3\times10^4 < Re < 2\times10^5$). The results showed a combination of both fast and slow turbulent components. The respective contributions of the fast and slow motions were quantified using a novel triple decomposition technique. The results highlighted the 'true' turbulent characteristics linked to the fast, microscopic velocity turbulence of hydraulic jumps, while showing that slow-fluctuation turbulence intensity was a significant contribution to the total. The high-frequency advection length scale and integral turbulent length scale exhibited some maxima in the lower shear flow next to the invert. The turbulent length scales decreased along the roller as the fast turbulence was dissipated. Comparison between the longitudinal advection and integral length scales indicated that the advection and diffusion were not independent processes in the flow region immediately downstream of the jump toe. The impact of slow fluctuations was large in the free-surface region and relatively smaller in the lower shear flow.

Keywords: Hydraulic jump, Turbulence, Air-water flow measurement, Triple decomposition, Free-surface dynamics

1. INTRODUCTION

A hydraulic jump forms at the sudden transition from a supercritical to subcritical flow. It is a turbulent two-phase flow with discontinuity in flow depth and velocity field at the jump toe (Leutheusser & Kartha 1972). The flow in the jump roller is extremely complex with the development of large-scale turbulence both at the free-surface and inside the roller. The fluctuating nature of the flow, such as the oscillation of jump toe position and production of large-size eddies, is visible in pseudo-periodic manner (Hoyt & Sellin 1989, Long et al. 1991). Microscopic turbulence exists meanwhile with much smaller time and length scales and mostly in randomness. Both macroscopic and microscopic turbulent processes interact with the entrainment and transport of air. Considering of the complexity arising with the coupling between almost all physical processes in wide ranges of length and time scales and the numerous parameters required describing all phenomena, our knowledge on hydraulic jumps is far from a full understanding. Physical modelling is to date the most reliable method to study this phenomenon, while recent development in numerical modelling of such breaking free-surface flows requires solid verification by supportive experimental data (Prosperetti & Tryggvason 2009, Lubin & Glockner 2013).

Direct measurements of air-water flow in hydraulic jump dated back to Rajaratnam (1962) who measured the void fraction and velocity distributions. Key contributions included but not limited to the work of Resch & Leutheusser (1972) highlighting the importance of inflow conditions and Chanson (1995) proposing an analogy of the air entrainment process in hydraulic jump with that in plunging jets. These experimental studies were facilitated with intrusive conductivity and hot-film anemometer phase-detection probes. The application of non-intrusive flow measurement techniques is limited to weak hydraulic jumps because most instruments are designed for mono-phase flow (Svendsen et al. 2000, Liu et al. 2004, Lennon & Hill 2006, Mignot & Cienfuegos 2010). For the strong hydraulic jumps with presence of large amount of air bubbles, the non-intrusive techniques were mostly restricted to imaging of full-field air distributions (Mossa & Tolve 1998, Leandro et al. 2012). Detailed turbulence characteristics were mainly derived based upon intrusive air-water interface detections and statistical data analysis (Chanson & Toombes 2002). Correlation analysis of two-point phase-detection signals enabled successful quantification of turbulence intensity and further turbulent length/time scales in the high-velocity bubbly flow (Chanson & Carosi 2007). However, because the statistical data processing does not discriminate the large-scale non-randomness in the flow motion, the characterization of micro-scale turbulence in hydraulic jump is adversely affected by the flow instabilities associated with the pseudo-periodic motions of free-surface and large vortical structures.

The most relevant studies of self-sustained flow instabilities were primarily focused on the free-surface dynamics. Previous experimental investigations encompassed Mouaze et al. (2005), Murzyn et al. (2007), Murzyn & Chanson (2009) and Chachereau & Chanson (2011). Either intrusive wire gauges or non-intrusive acoustic displacement meters were used to analyze the surface fluctuations and characteristic frequencies. The translation of hydraulic jump position was examined by Mossa (1999), and observation of jump toe oscillation was reported in Zhang et al. (2013). A recent numerical simulation was conducted by Richard & Gavrilyuk (2013) modelling the free-surface fluctuations and jump toe oscillations. The computational results further indicated jump toe oscillation frequencies independent of the distance to the downstream boundary (Richard 2013). Although some discussions on the correlation between the void fraction, free-surface fluctuation and turbulence intensity were proposed for breaking waves and weak hydraulic jumps (Peregrine & Svendsen 1978, Cox & Shin 2003, Longo 2011), no investigation considered the impact of flow instabilities on turbulence characterization for strong hydraulic jumps with substantial air entrainment and intense free-surface deformation up to date.

This paper presents new experiments on air-water flow and turbulence measurements using phase-detection probes. Turbulence properties were deduced from interface-detection signals, including the turbulence intensity, advection length scale, and integral turbulent length and time scales in both longitudinal and transverse directions. The experimental data showed some unusual large turbulent levels and turbulent scales, which was believed to be linked with the pseudo-periodic motions of the flow. A triple decomposition technique developed by Felder & Chanson (2014) was applied to the non-stationary air-water flows, to identify the true turbulent scales of the flow. Herein the triple decomposition technique was applied to the hydraulic jump flow to quantify the turbulent flow contributions linked with the fast and slow fluctuating velocity components. The results validated the application of this technique to hydraulic jumps, and showed significant influence of the flow instabilities. The findings provided an improved quality of turbulence characterization for such a complex air-water flow.

2. INSTRUMENTATION, DATA PROCESSING AND FLOW CONDITIONS

Hydraulic jumps were generated in a 3.2-m long horizontal channel with a rectangular cross-section of 0.5-m wide × 0.41-m high. Water was supplied from a constant head reservoir into the upstream head tank of the channel (Fig 1). The flow rate was measured with a Venturi meter mounted in the supply pipeline with an accuracy of ±2%. The undershoot rounded gate (Ø = 0.3 m) of the head tank induced a horizontal impinging flow into the flume, and the downstream flow conditions were controlled with an overshoot sluice gate at the end of the channel. The inflow depth d_1 was measured with a pointer gauge, the accuracy mainly dependent upon the free-surface roughness with uncertainties up to ±5%.

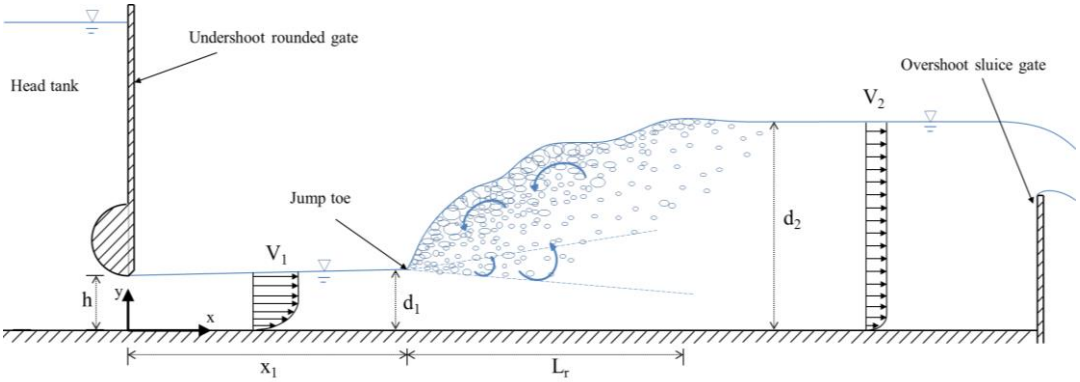

Figure 1. Sketch of experimental channel and basic parameters of a hydraulic jump

The presence of large amount of air bubbles hindered the application of most non-intrusive turbulence measurement techniques. A robust instrument, successfully used for decades, is the intrusive conductivity phase-detection probe (Rajaratnam 1962, Chanson & Carosi 2007). Each phase-detection probe was equipped with two 0.25-mm inner diameter needle sensors. The needle sensor detected the air-water interfaces according to the different electrical resistance of air and water. The two sensors were sampled simultaneously at 20 kHz for 45 s.

The phase-detection probe signal exhibited a bimodal voltage probability distribution, with two distinctive peaks corresponding to the detection of air and water phases respectively. An air-water threshold was selected at 50% between the two peak voltage probabilities, and all sample points in the raw signal were converted to instantaneous void fraction c, where c = 0 for water and c = 1 for air. The time-averaged void fraction C represented the volume of air per unit volume of air and water, and the bubble count rate F, defined as the number of air bubbles or water droplets per unit time, was deduced.

When the two sensors of phase-detection probe were aligned with the flow direction and separated with a longitudinal distance Δx between the tips (Fig 2a), statistical turbulence properties were derived based upon some correlation analysis of the probe signals. Denoting the leading sensor signal as x and the trailing sensor signal as x', Figure 3 sketches typical shapes of the auto-correlation function $R_{xx}(\tau)$ for the leading signal and cross-correlation function $R_{xx'}(\tau)$ between the leading and trailing signals, where τ is the time lag between the correlated datasets, T is the time lag of maximum cross-correlation coefficient, $T_{0.5}$ and $\tau_{0.5}$ are respectively the relative time lags of half maximum auto-correlation and cross-correlation, i.e. $R_{xx}(T_{0.5}) = 0.5$ and $R_{xx'}(T+\tau_{0.5}) = (R_{xx'})_{max}/2$. The time-averaged air-water interfacial velocity, considered equivalent to the flow velocity, was calculated as

$$V = \frac{\Delta x}{T} \quad [1]$$

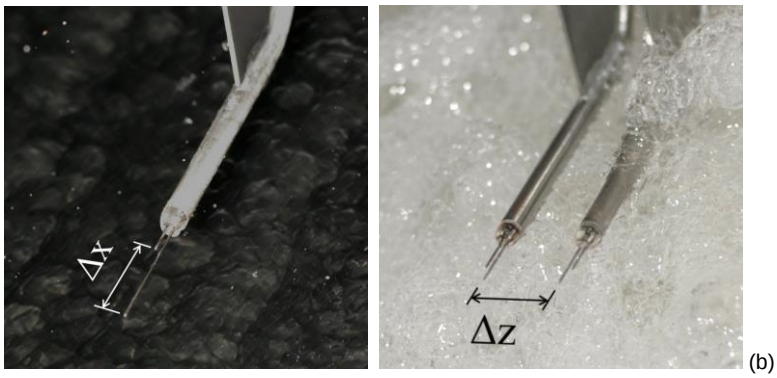

(a) (b)

Figure 2. Double-tip conductivity phase-detection probes: (a, left) Leading and trailing probe sensors separated with a longitudinal distance Δx; (b, right) Leading sensors of side-by-side probes separated with a transverse distance Δz

Herein the characteristic time lag T indicated the average interfacial travel time between the sensor tips. The turbulence intensity Tu = v'/V was estimated within some key assumptions. First, it was assumed that the successive detection of air-water interfaces by the phase-detection probe was a true random process, thus the correlation functions followed a Gaussian distribution, leading to the standard deviations of the auto-correlation and cross-correlation functions as $T_{0.5}/1.175$ and $\tau_{0.5}/1.175$ respectively (Chanson & Toombes 2002). Second, it was assumed that the number of air-water interfaces n was infinitely large, and the average interfacial travel time T satisfied that

$$\frac{1}{T} \times \sqrt{\sum_{i=1}^{n} (t_i - T)^2 \Big/ n^2} = \sqrt{\sum_{i=1}^{n} \left(\frac{t_i - T}{t_i}\right)^2 \Big/ n^2} \quad [2]$$

where t_i (i = 1, …, n) is the instantaneous interfacial travel time. The right hand side of Eq. [2] yielded to the total turbulence intensity v'/V, while the approximation Tu was derived from the left hand side based upon the first assumption:

$$Tu = 0.851 \times \frac{\sqrt{\tau_{0.5}^2 - T_{0.5}^2}}{|T|} \quad [3]$$

Note that the estimate of Tu was dependent upon the broadening of cross-correlation function, and hence was a function of the longitudinal separation of the phase-detection probe sensors Δx.

An auto-correlation time scale T_{xx} and cross-correlation time scales $T_{xx'}$ and T_{xz} were calculated as

$$T_{xx} = \int_{0}^{\tau(R_{xx'}=0)} R_{xx}(\tau) \times d\tau \quad [4]$$

$$T_{xx'} = \int_{T}^{\tau(R_{xx'}=0)} R_{xx'}(\tau) \times d\tau \quad [5]$$

$$T_{xz} = \int_{\tau(R_{xz}=(R_{xz})_{max})}^{\tau(R_{xz}=0)} R_{xz}(\tau) \times d\tau \quad [6]$$

T_{xx} and $T_{xx'}$ are illustrated in Figure 3, while T_{xz} was derived from the cross-correlation function $R_{xz}(\tau)$ between the synchronous signals of two side-by-side phase-detection probe sensors with the same longitudinal and vertical locations but a transverse separation Δz (Fig 2b). The auto-correlation time scale T_{xx} is a measure of the characteristic advective time of bubbly flow structures (e.g. eddies advecting the air-water interfaces) in the streamwise direction. It further gave the advection length scale L_{xx}:

$$L_{xx} = V \times T_{xx} \quad [7]$$

The advection length scale L_{xx} is a characteristic longitudinal size of advecting eddies (Chanson & Carosi 2007). The cross-correlation time scales $T_{xx'}$ and T_{xz} were functions of the probe tip separations Δx and Δz. When the measurements were repeated for a range of separation distances, the integral turbulent length and time scales were further calculated in the longitudinal direction:

$$L_X = \int_{0}^{\Delta x((R_{xx'})_{max}=0)} (R_{xx'})_{max} \times d(\Delta x) \quad [8]$$

$$T_X = \frac{1}{L_X} \times \int_{0}^{\Delta x((R_{xx'})_{max}=0)} (R_{xx'})_{max} \times T_{xx'} \times d(\Delta x) \quad [9]$$

and in the transverse direction:

$$L_Z = \int_0^{\Delta z((R_{xz})_{max}=0)} (R_{xz})_{max} \times d(\Delta z) \quad [10]$$

$$T_Z = \frac{1}{L_Z} \times \int_0^{\Delta z((R_{xz})_{max}=0)} (R_{xz})_{max} \times T_{xz} \times d(\Delta z) \quad [11]$$

The integral length and time scales give some measure of the inherent turbulent scales of large vortical structures in the longitudinal and transverse directions respectively (Chanson & Carosi 2007). In the flow region with separate and additive advection and diffusion processes, it would be expected that the advection and integral turbulent length scales are about equal in the longitudinal direction: $L_{xx} \approx L_X$.

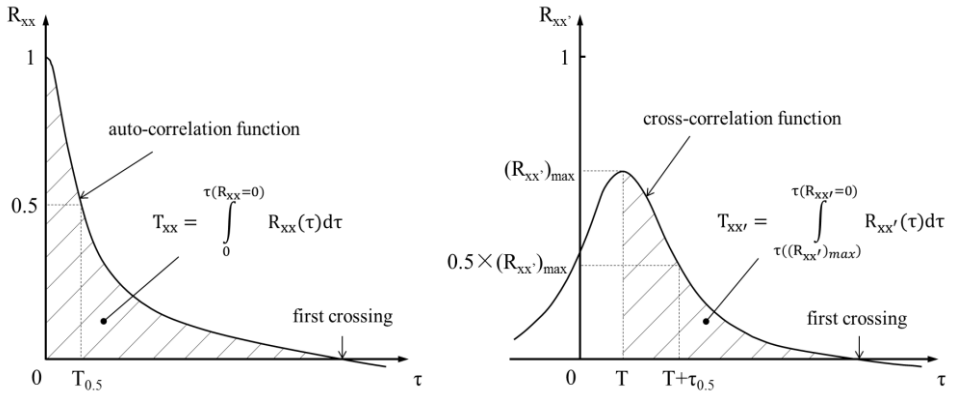

Figure 3. Definition sketch of auto-correlation and cross-correlation functions of phase-detection probe signals

The experiments were conducted with three inflow Froude numbers Fr_1 = 3.8, 5.1 and 7.5 and two intake aspect ratios h/W = 0.04 and 0.06. The flow conditions are summarized in Table 1. Partially-developed inflow conditions were applied to all experimental flows. Measurements were performed on the channel centerline, through three to five vertical cross-sections depending upon the length of the jump. The longitudinal and transverse integral turbulent length/time scales were only obtained with repeated measurements for the flow condition Fr_1 = 7.5, Re = 6.6×10^4 & h/W = 0.04. Different separation distances between phase-detection probe sensors, Δx in longitudinal and Δz in transverse direction, were applied and summarized in Table 2.

Table 1. Experimental flow conditions

	Q [m^3/s]	W [m]	h [m]	x_1 [m]	d_1 [m]	V_1 [m/s]	L_r [m]	Fr_1 [-]	Re [-]
	0.0170	0.5	0.020	0.83	0.020	1.70	0.28	3.8	3.4×10^4
	0.0226				0.020	2.26	0.52	5.1	4.5×10^4
*	0.0333				0.020	3.33	0.80	7.5	6.6×10^4
	0.0342	0.5	0.030	1.25	0.032	2.14	0.60	3.8	6.8×10^4
	0.0460				0.032	2.88	0.85	5.1	9.1×10^4
	0.0706				0.033	4.28	1.45	7.5	1.4×10^5

Notes: Q: flow rate; W: channel width; h: upstream gate opening; x_1: longitudinal jump toe position; d_1: inflow depth; V_1: average inflow velocity; L_r: roller length; Fr_1: inflow Froude number; Re: inflow Reynolds number; *: integral turbulent length/time scale measurements

Table 2. Separation distances between two phase-detection probe sensor tips for the measurement of longitudinal and transverse integral turbulent scales with flow conditions Fr_1 = 7.5, Re = 6.6×10^4 and h/W = 0.04

Turbulent properties	Δx [mm]	Δz [mm]
L_X, T_X	2.57, 5.0, 7.25, 9.28, 13.92, 29.68	2.0
L_Z, T_Z	0	0.9, 3.6, 9.0, 17.1, 27.0, 36.6, 49.2, 92.0

Notes: L_X, T_X: longitudinal integral turbulent length/time scale; L_Z, T_Z: transverse integral turbulent length/time scale; Δx, Δz: longitudinal/transverse separation distance between the phase-detection probe sensors

3. TWO-PHASE FLOW MEASUREMENT RESULTS

3.1 Flow patterns and self-sustained instabilities

The characteristic dimensions of hydraulic jump, including the ratio of conjugate depths d_2/d_1, the relative jump roller length L_r/d_1 and time-averaged free-surface profile, were found to be functions of the inflow Froude number and almost independent of the Reynolds number. The jump roller was primarily characterized with intense turbulence developing both at the free-surface and inside the roller, major air entrainment at the jump toe and convective transport of air bubbles in the turbulent shear region. Self-sustained instabilities were visible with free-surface fluctuations and splashing

downstream propagation of surface waves, longitudinal jump toe oscillations, fluctuations of transverse impingement perimeter, and successive formation of large-scale vortices in which the entrapped air was advected downstream. These pseudo-periodic motions are illustrated in a side-view image of jump roller in Figure 4. The motions interacted with each other, and all contributed to the low-frequency fluctuations of the flow. The characteristic frequencies were observed and measured with non-intrusive water surface detections in several previous studies (Chanson 2006,2010, Murzyn & Chanson 2009, Chachereau & Chanson 2011, Zhang et al. 2013, Wang & Chanson 2014). The findings are summarized in Table 3. All comparative studies in Table 3 were performed with flumes of the same length, and the tailwater length downstream of jump roller had little impact on the frequencies of the fluctuating motions. All experimental data showed comparable frequency ranges for jump toe oscillations and vortex advections between 0.4 and 2 Hz, while the free-surface fluctuation frequencies were between 0.8 and 4 Hz. The Strouhal number of the jump toe frequencies $f \times d_1/V_1$ was suggested to decrease with increasing inflow Froude number (Wang & Chanson 2014).

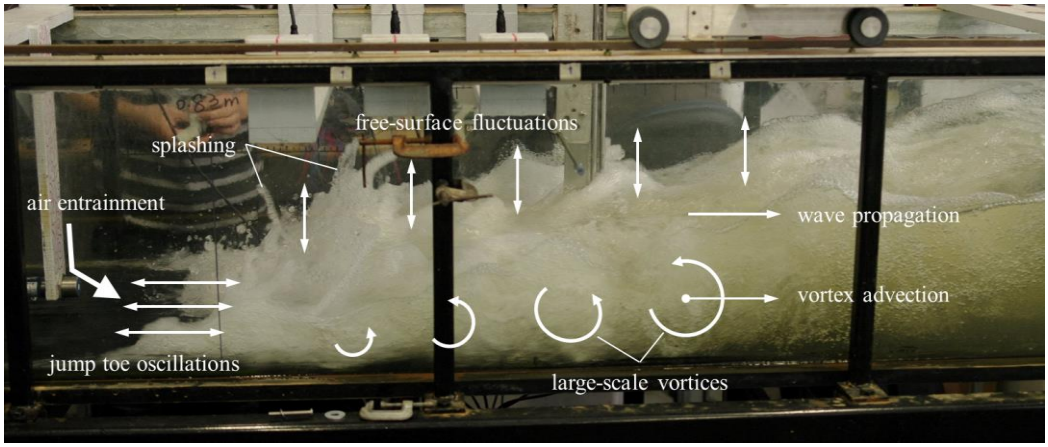

Figure 4. Macroscopic fluctuating motions in hydraulic jump roller – Flow conditions: Q = 0.0347 m^3/s, d_1 = 0.0208 m, x_1 = 0.83 m, Fr_1 = 8.5, Re = 8.0×10^4

Table 3. Characteristic frequency ranges of pseudo-periodic motions in hydraulic jump

Motions of flow	Reference	Method	Frequency range [Hz]
Free-surface fluctuations	Murzyn & Chanson (2009)	Acoustic displacement meter measurement	0.8 to 4.0
	Chachereau & Chanson (2011)	Acoustic displacement meter measurement	1.6 to 3.9
	Wang & Chanson (2014)	Acoustic displacement meter measurement	1.2 to 3.7
Jump toe oscillations	Chanson (2006)	Visual observation	0.6 to 2.0
	Murzyn & Chanson (2009)	Visual observation	0.5 to 0.8
	Chanson (2010)	Visual observation	0.4 to 0.8
	Zhang et al. (2013)	Visual observation	0.7 to 1.4
	Wang & Chanson (2014)	Acoustic displacement meter measurement	0.5 to 1.3
	Richard & Gavrilyuk (2013)	Numerical simulation	0.2 to 1.1
Large vortex advections	Chanson (2010)	Visual observation	0.4 to 1.1
	Zhang et al. (2013)	Visual observation	0.4 to 1.4

3.2 Basic air-water flow properties

The distributions of time-averaged void fraction C and bubble count rate $F \times d_1/V_1$ on the channel centerline are presented in Figures 5a and 5b for the aspect ratio h/W = 0.06. The roller surfaces are outlined at the elevation Y_{90} where C = 0.9. The void fraction reflected the extent of the flow aeration, while the bubble count rate was further linked with the number and average size of bubbles as well as the total air-water interfacial area, which was largely determined by the local shear stress. The data profiles highlighted two flow regions in the jump roller, namely the turbulent shear region on the bottom and the recirculation region above, the boundary in between being characterized with a trough void fraction (also a trough bubble count rate). Both void fraction and bubble count rate exhibited local maxima in the shear flow, but at different elevations. The local maximum values C_{max} and F_{max}, as well as the depth-averaged values, decreased along the roller for each flow. Comparison between the experimental data with the same Froude number but different aspect ratios showed larger bubble count rate for a higher Reynolds number (not shown) because, for a given void fraction, the number of bubbles was determined by the shear stress linked with the turbulence level of the flow. In the free-surface recirculation region, the void fraction increased rapidly to unity, and a secondary peak in bubble count rate profile was shown for C = 0.3 to 0.4. The typical data distributions applied to all flow conditions and were consistent with the previous investigations (Murzyn & Chanson 2009, Chanson 2010, Chachereau & Chanson 2011).

Figures 6a and 6b present respectively the interfacial velocity and turbulence intensity distributions for the same flow conditions in Figures 5a and 5b. The velocity profiles showed positive average velocity in the shear region with longitudinal deceleration and almost uniform negative velocity for the reversed free-surface flow. The turbulence intensity Tu increased monotonically with increasing elevation in the positive flow region. In Figure 6, Tu represents the total turbulence intensity. When negative instantaneous velocity started to appear (though the average velocity could be still positive), the turbulence level increased significantly, sometimes yielding physically meaningless turbulence intensities Tu > 3 to 4. This was attributed to the inclusion of macroscopic fluctuating motions in the microscopic turbulence

characterization. The velocity fluctuations encompassed the components caused by the free-surface deformations and jump toe oscillations which were much larger in length and time scales compared to the "true" velocity turbulence. Detailed quantification will be given in the Discussion section.

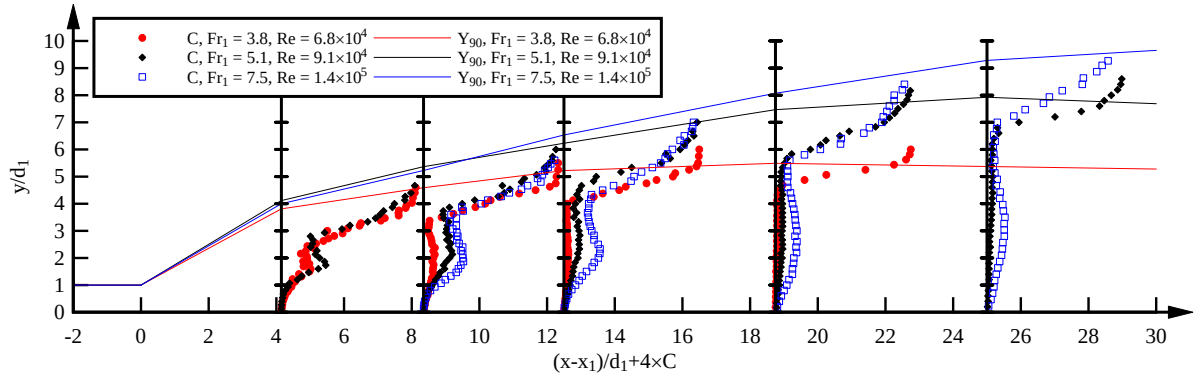

(a) Time-averaged void fraction, h/W = 0.06

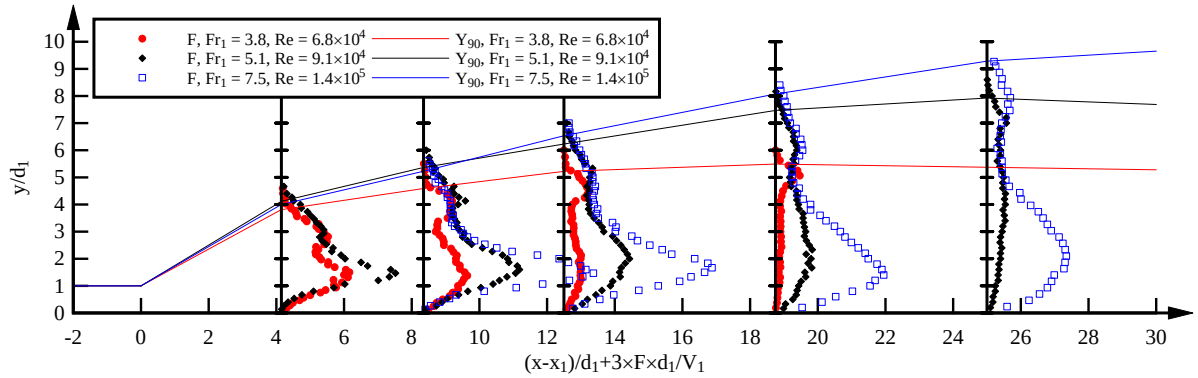

(b) Bubble count rate, h/W = 0.06

Figure 5. Time-averaged void fraction and bubble count rate distributions in hydraulic jumps

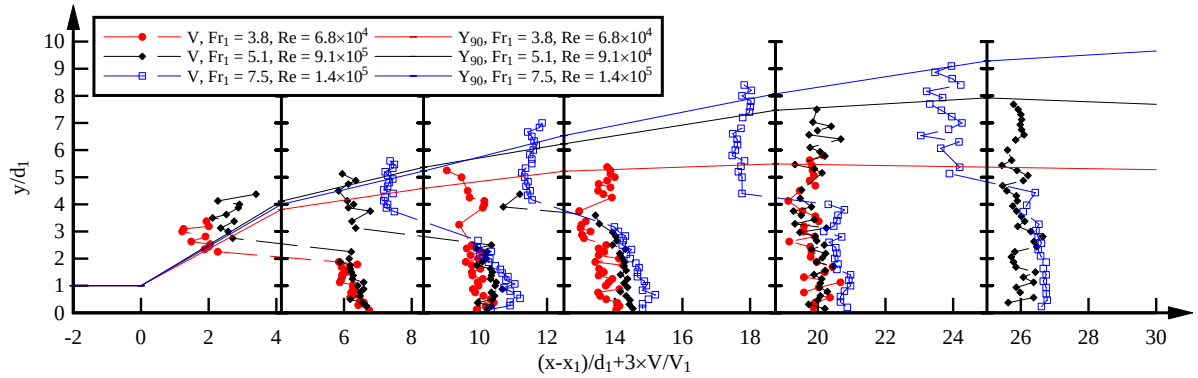

(a) Time-averaged void fraction, h/W = 0.06

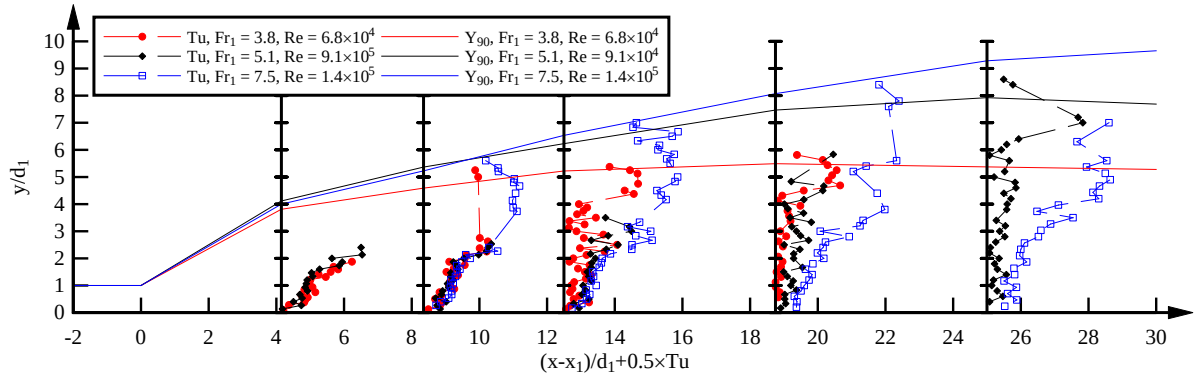

(b) Turbulence intensity, h/W = 0.06

Figure 6. Time-averaged air-water interfacial velocity and turbulence intensity distributions in hydraulic jumps

3.3 Turbulent length and time scales

The longitudinal advection length scale L_{xx}, calculated with the auto-correlation time scale T_{xx} and interfacial velocity V (Eq. [7]), is compared with the longitudinal integral turbulent length scale L_X given by the integration of characteristic lengths equalling Δx weighted by the corresponding maximum correlation coefficients (Eq. [8]). The results are shown in Figure 7a. The transverse integral length scale L_Z is also presented. All dimensionless length scales were shown in the same order of magnitude (~10^{-2} m). It indicated that turbulent structures of comparable sizes developed both along and perpendicular to the main flow direction.

In the mixing shear layer, turbulent flow structures of various dimensions formed and were advected. The advection length scale L_{xx} represented some average dimension of these advecting structures, while the integral turbulent length scale L_X provided a statistic measure over a range of characteristic sizes in the streamwise direction. Both length scales were closely linked with the entrained air bubbles carried in these vortical structures. In the shear flow region, the experimental data showed larger integral length scale L_X than the advection length scale L_{xx} within a short distance downstream of the jump toe. It implied strong advecting processes exerted on a wide range of eddy sizes, especially for the large-size turbulent structures. The diffusion process was highly affected by the advective transportation, implying that Taylor's hypothesis of $L_{xx} \approx L_X$ for separate and additive diffusion and advection processes was not satisfied. Close length scales were achieved at further downstream positions in the lower flow region, associated with dissipation of large turbulent structures and separation of advective and diffusive processes.

The integral turbulent time scales T_X and T_Z are presented in Figure 7b. Similar data distributions were shown between longitudinal and transverse time scales. The results gave a measure of characteristic time scales of the air advection in large turbulent structures, which were in an order of magnitude of 10^{-3} s in the lower shear region and of 10^{-2} s near the free-surface.

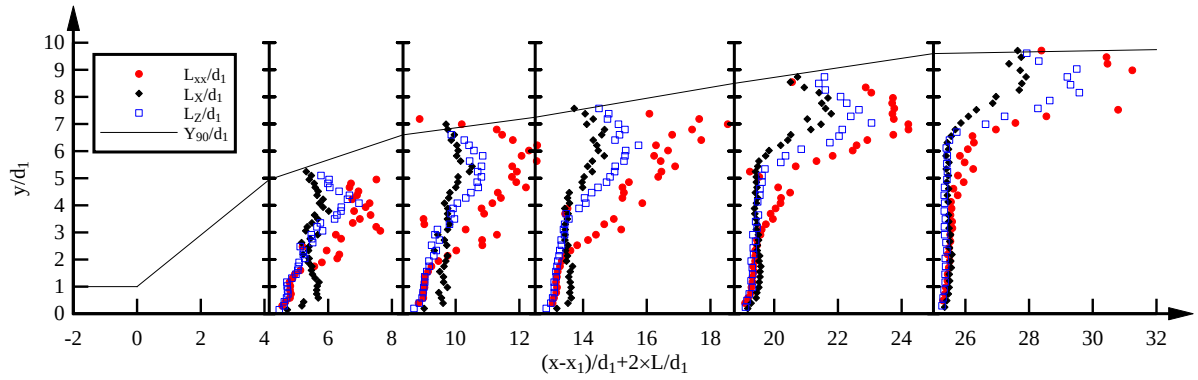

(a) Dimensionless advection length scale L_{xx}, longitudinal integral turbulent length scale L_X & transverse integral turbulent length scale L_Z

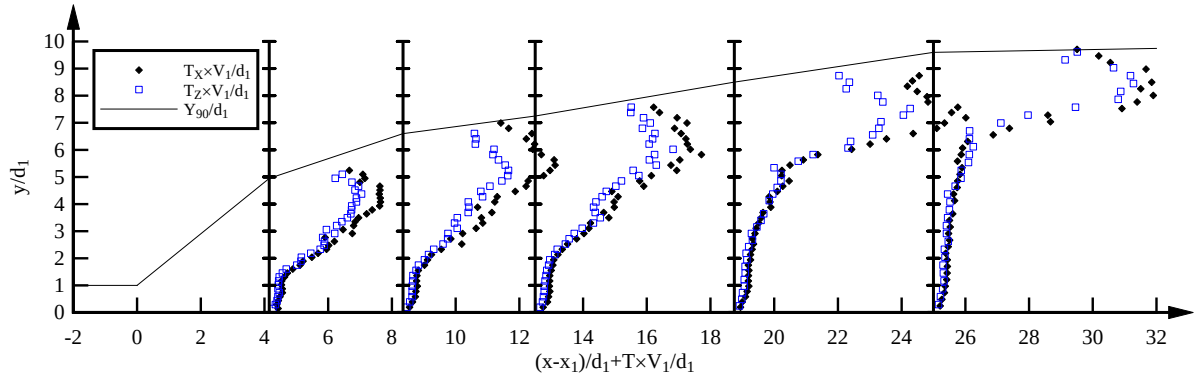

(b) Dimensionless longitudinal and transverse integral turbulent time scales T_X & T_Z

Figure 7. Distributions of turbulent length and time scales in longitudinal and transverse directions in hydraulic jumps – Flow conditions: Q = 0.0333 m^3/s, d_1 = 0.02 m, x_1 = 0.83 m, Fr_1 = 7.5, Re = 6.6×10^4

4. DISCUSSION: DECOMPOSITION OF TURBULENT PROPERTIES

The correlation analysis of raw phase-detection probe signals yielded large and scattered turbulent flow properties in the free-surface region linked to the effects of macroscopic free-surface dynamics (Fig 6 & 7). A decomposition of the signals allowed for identification of respective contributions of the low-frequency and high-frequency motions. The raw signal was decomposed into an average component, a low-frequency component corresponding to the slow fluctuations and a high-frequency component corresponding to the fast turbulent motions (Felder & Chanson 2014). The frequency thresholds between signal components were selected with reference to the characteristic frequency ranges of the pseudo-periodic motions. For example, experimental observations and measurements suggested typical frequency ranges from 0.4 to 4

Hz for free-surface fluctuations, jump toe oscillations and large-size vortex advections (Table 3). The findings applied to a wide range of flow conditions. In addition, spectral analysis of the raw signal further suggested some characteristic frequency ranges between 0.3 – 0.5 Hz and 10 – 15 Hz, and between 10 – 15 Hz and > 100 Hz in the signal. The lower range was thought to reflect the impact of flow instabilities, whereas the higher range corresponded to the detection of most air bubbles (Wang et al. 2014). Overall, both experimental observations and spectral analysis suggested the frequencies of slow fluctuations in an order of 10^{-1} to 1 Hz. Herein the lower and upper cut-off frequencies of the slow fluctuations were set at 0.33 and 10 Hz respectively. Motions with frequencies lower than 0.33 Hz were considered as the mean components and those above 10 Hz were classified as high-frequency components. The selection was supported by a sensitivity study of cut-off frequencies by Felder (2013) for a similar hydraulic jump configuration.

A triple decomposition of instantaneous void fraction was performed thereafter with low-pass, band-pass and high-pass filtering (Felder & Chanson 2014):

$$c = \bar{c}+c'+c'' \quad [12]$$

where $\bar{c}$ is a mean void fraction, c' and c'' are respectively the low-frequency and high-frequency components. Eq. [12] led to the decomposition of time-averaged void fraction $C = \bar{C}+C'+C''$, for which $\bar{C} \approx C$ and $C' \approx C'' \approx 0$. For the selected frequency thresholds, most bubble count rates satisfied the relationships $F'' \approx F$, $\bar{F} \approx F' \approx 0$.

The decomposition of correlation functions was a linear process. The decomposed correlation functions were proportional to the correlation functions between the filtered signal components, with absence of time-averaged components in the results (Felder 2013). Therefore, most turbulence properties were obtained for the filtered signal components with the decomposed correlation functions. The decomposed time-averaged velocities were given by $V' = \Delta x/T'$ and $V'' = \Delta x/T''$, where T' and T'' are time lags for the corresponding maxima of decomposed low-frequency and high-frequency cross-correlation functions respectively. The experimental data suggested $T' \sim T'' \approx T$ hence $V' \sim V'' \approx V$. An example can be seen in Figure 8, showing the distributions of V, V' and V'' in a vertical cross-section with comparison to the best fit wall jet solution (Chanson 2010). The coincidence between V and V'' was linked to the sequential detection of air-water interfaces with two phase-detection probe sensors being a high-frequency process (Felder & Chanson 2014). For a flow velocity between 1 and 5 m/s, the typical interfacial travel time between the sensor tips (5 mm < Δx < 10 mm) was between 1 and 10 ms, corresponding to a characteristic frequency from 100 to 1000 Hz, one to two orders of magnitude higher than the upper decomposition cut-off frequency. On the other hand, the low-frequency signal component provided less accurate estimate of T' with a broad, flat peak in the decomposed cross-correlation function (not shown here).

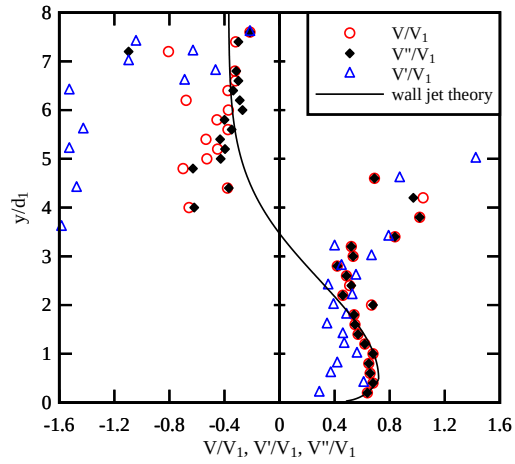

Figure 8. Decomposition of interfacial velocity in a vertical cross-section of jump roller – Flow conditions: Q = 0.0333 m^3/s, d_1 = 0.02 m, x_1 = 0.83 m, Fr_1 = 7.5, Re = 6.6×10^4; $(x-x_1)/d_1$ = 12.5

The correlation time scales can be expressed as the sum of the decomposed terms (e.g. $T_{xx} \approx T_{xx}'+T_{xx}''$, $T_{xx'} \approx T_{xx'}+T_{xx'}''$), each term being integrated with the corresponding decomposed correlation functions. For the advection length scale and longitudinal integral turbulent length/time scales, the high-frequency components were calculated as:

$$L_{xx}'' = V''\times T_{xx}'' \quad [13]$$

$$L_X'' = \int_0^{\Delta x((R_{xx'}'')_{max}=0)} (R_{xx'}'')_{max}\times d(\Delta x) \quad [14]$$

$$T_X'' = \frac{1}{L_X''}\times \int_0^{\Delta x((R_{xx'}'')_{max}=0)} (R_{xx'}'')_{max}\times T_{xx'}''\times d(\Delta x) \quad [15]$$

where $(R_{xx'}'')_{max}$ is the maximum of decomposed cross-correlation function $R_{xx'}''$ which is proportional to the cross-correlation function between the high-frequency signal components. The low-frequency components were obtained in similar ways. Figure 9a presents the advection and integral turbulent length scales for both raw and filtered signals in the same cross-section, including the void fraction profile. Both high-frequency decomposed length scales were significantly smaller than those of raw signal and low-frequency signal component, especially in the upper shear flow and entire free-surface region where each high-frequency length scale was nearly uniform. It implied that the large length scales of raw signal were mainly induced by the low-frequency motions in the flow, with the largest impact next to the free-surface. In

the lower shear flow, both high-frequency length scales exhibited maxima, $(L_{xx}")_{max}$ and $(L_X")_{max}$, and the integral length scale $L_X"$ was consistently larger than the advection length scale $L_{xx}"$. This is illustrated in Figure 9b. The shape of vertical distribution reflected the existence of high-frequency turbulent structures in the lower shear flow, which were rarely seen in the upper flow region. The low vertical positions of these turbulent structures were in agreement with the observations showing the interaction between the shielding of large vortices and the channel bed. Figure 9b also shows decreases in both maximum length scales with increasing distance from the jump toe. The longitudinal decay of $(L_{xx}")_{max}/d_1$ and $(L_X")_{max}/d_1$ is shown in Figure 9c for the given flow condition (Fr_1 = 7.5, Re = 6.6×10^4), with the data correlated as:

$$\frac{(L_{xx}")_{max}}{d_1} = 0.28\times\exp\left(-0.038\times\frac{x-x_1}{d_1}\right) \quad [16]$$

$$\frac{(L_X")_{max}}{d_1} = 0.79\times\exp\left(-0.057\times\frac{x-x_1}{d_1}\right) \quad [17]$$

Though the size of large vortices was observed to increase along the roller, the decreasing turbulent length scales indicated the dissipation of high-frequency turbulent structures which acted a more predominant role. $L_{xx}"$ and $L_X"$ were expected to be equal at further downstream positions in the quasi-uniform subcritical flow, and both ultimately decreased to zero as the high-frequency turbulence is fully dissipated.

The decomposition of length scales showed the relationships $L_{xx} \sim L_{xx}'+L_{xx}"$ and $L_X \approx L_X'+L_X"$. The scattered low-frequency advection length scale L_{xx}' was related to the scattered low-frequency velocity component V'. Comparison between the two length scales indicated different relationships in the upper and lower flow regions, i.e., $L_{xx} > L_X$, $L_{xx}' > L_X'$, $L_{xx}" \approx L_X"$ for $y > y(C = C_{max})$, and $L_{xx} < L_X$, $L_{xx}' \approx L_X'$, $L_{xx}" < L_X"$ for $0 < y < y(C = C_{max})$ (Fig 9a). It implied that the difference in the advection and integral length scales of raw signal was mainly caused by the slow fluctuations in the upper flow and by the fast turbulent motions in the lower flow region. In the lower shear flow, the larger integral length scale than advection length scale reflected strong and fast advection of relatively large turbulent structures in the longitudinal direction.

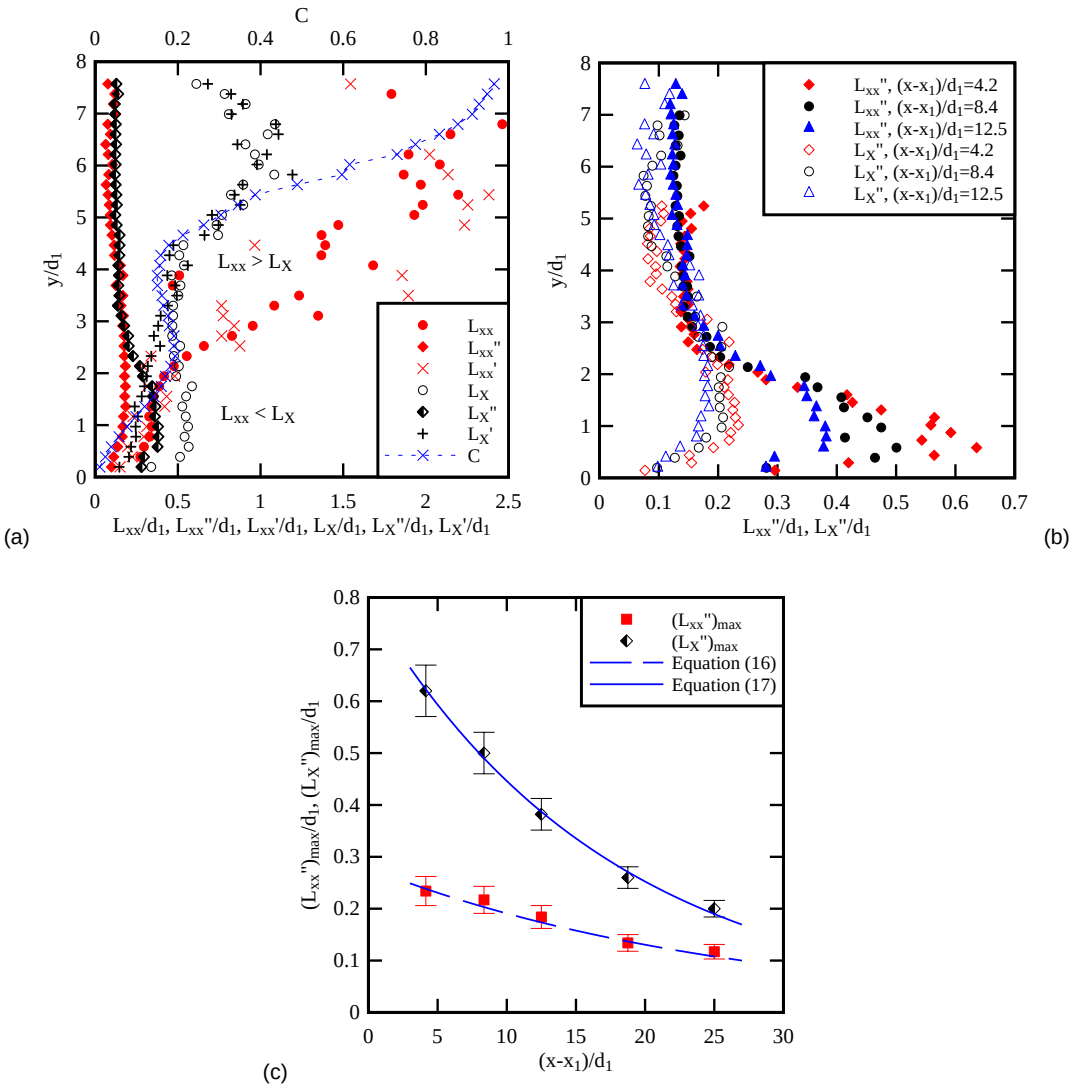

Figure 9. Decomposition of longitudinal advection length scale L_{xx} and integral turbulent length scale L_X – Flow conditions: Q = 0.0333 m^3/s, d_1 = 0.02 m, x_1 = 0.83 m, Fr_1 = 7.5, Re = 6.6×10^4. (a, top left) Decomposition of longitudinal advection and integral turbulent length scales at $(x-x_1)/d_1$ = 12.5; (b, top right) Longitudinal advection length scale and integral turbulent length scale for high-frequency signal

components at different longitudinal positions; (c, bottom) Longitudinal distribution of maximum advection length scale and integral turbulent length scale for high-frequency signal components

The decomposition results of longitudinal integral turbulent time scale T_X are shown in Figure 10, with close integral time scales of raw and low-frequency signals ($T_X \approx T_X'$). The high-frequency integral time scale T_X'' was one order of magnitude smaller than T_X and T_X' in the upper flow region. The data suggested an approximate relationship $T_X \approx T_X'+T_X''$. Figure 10b shows the distribution of T_X'' at five longitudinal positions. In the lower shear flow, the high-frequency integral time scale exhibited a peak value at the first three cross-sections. Both the maximum and the depth-averaged integral time scales decreased in the downstream direction, reflecting the shortening of a characteristic "lifetime" of high-frequency turbulent structures.

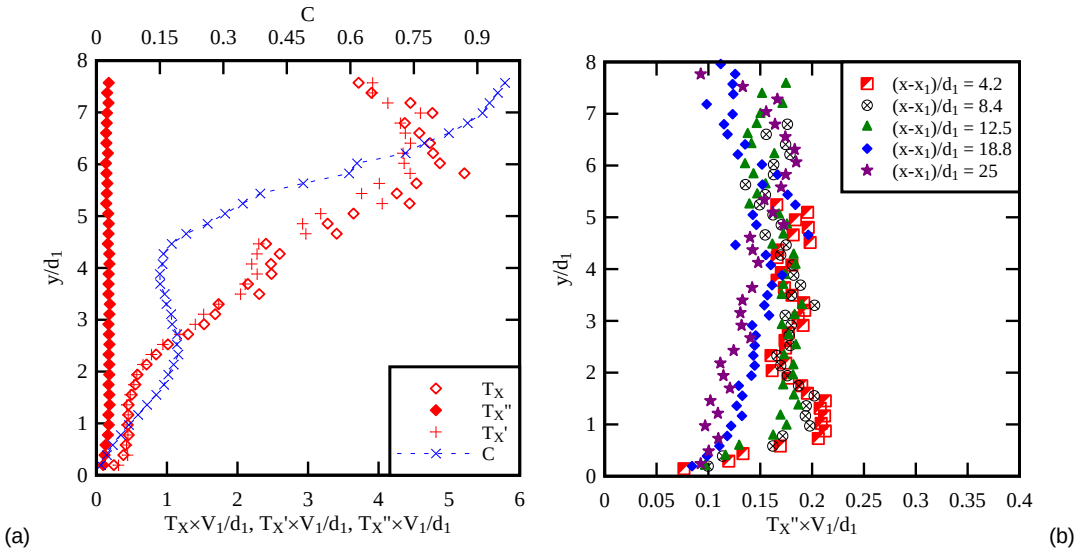

Figure 10. Decomposition of longitudinal integral turbulent time scale T_X – Flow conditions: Q = 0.0333 m^3/s, d_1 = 0.02 m, x_1 = 0.83 m, Fr_1 = 7.5, Re = 6.6×10^4. (a, left) Decomposition of longitudinal integral turbulent time scale at $(x-x_1)/d_1$ = 12.5; (b, right) Longitudinal integral turbulent length scale for high-frequency signal component at different longitudinal positions

Lastly, let us consider the decomposition of turbulence intensity Tu. It is noteworthy that the calculation of turbulence intensity Tu (Eq. [3]) is a non-linear process, thus the low-frequency and high-frequency components Tu' and Tu" could not be simply derived from the corresponding correlation functions. However, the experimental results on stepped spillway flow supported a relationship Tu ≈ Tu'+Tu" (Felder & Chanson 2014). Comparison between stepped spillway flows with and without instabilities showed comparable turbulence intensities deduced from the raw signal of the stable flow and from the high-frequency signal component of the instable flow. That is, the high-frequency signal component gave agreeable turbulence intensity with absence of the impact of flow instabilities. Herein the relationship Tu ≈ Tu'+Tu" was applied, where the decomposed terms Tu' and Tu" were calculated in the form of Eq. [3] with relevant parameters derived from corresponding correlation functions. The results are shown in Figure 11a for a specified cross-section and in Figure 11b comparing the whole datasets of Tu and Tu". Figure 11a shows comparable turbulence intensities Tu ≈ Tu' given by the raw signal and low-frequency signal component, with large values in the upper part of roller, whereas the high-frequency signal component yielded smaller, less scattered turbulence intensity Tu" through the vertical cross-section. Tu" showed some constant level of magnitude in both shear flow and recirculation region. In a thin layer between the two flow regions, Tu" was larger, because the local flow direction changed frequently with successive advection of large vortices, and the time-averaged velocity was small and close to zero. The data distribution was typical in the first half roller for all flow conditions. Figure 11b plots all Tu and Tu" in the first half roller at the relative elevation y/Y_{90}, showing Tu" mainly between 0.5 and 1.5.

A comparison between different flow conditions suggested that Tu" increased with increasing Reynolds number but was almost independent of Froude number. The results were larger than the findings of Resch & Leutheusser (1972) and Liu et al. (2004) who measured turbulence intensities no larger than 0.8, though their Froude numbers were restricted between 2 and 6 and their hydraulic jumps were constrained physically (Liu et al. 2004). In Figure 11b, a few scattered data points with large Tu" were seen in the upper flow region, because meaningless correlation functions were sometimes obtained for the raw signal, which could not be addressed by the signal decomposition technique. In the second half roller, Tu" decreased to between 0 and 0.7 as the high-frequency turbulence was largely dissipated.

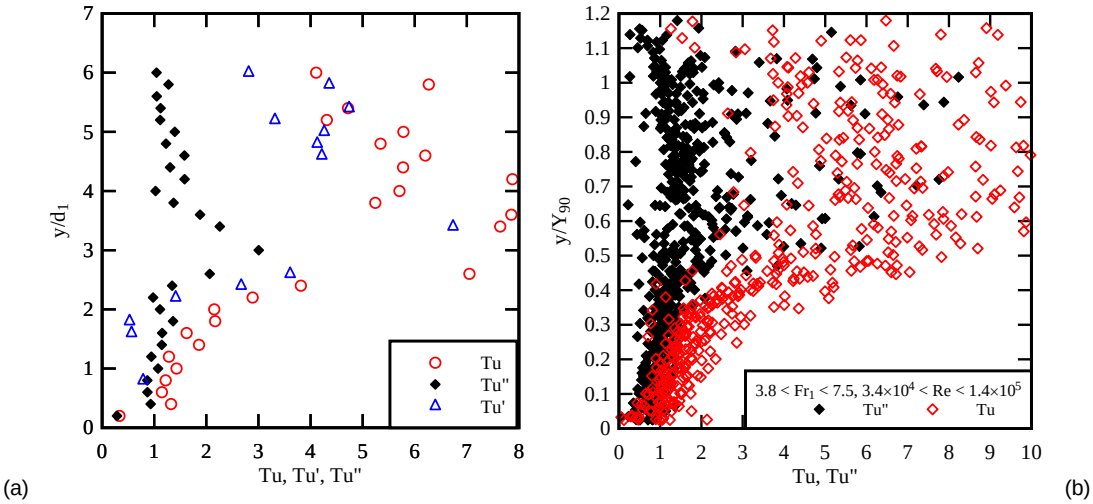

Figure 11. Decomposition of turbulence intensity: (a, left) Turbulence intensity for raw and filtered signals in a vertical cross section – Flow conditions: Q = 0.0333 m^3/s, d_1 = 0.02 m, x_1 = 0.83 m, Fr_1 = 7.5, Re = 6.6×10^4; $(x-x_1)/d_1$ = 8.35; (b, right) Comparison between turbulence intensities of raw signal and fast fluctuating signal component in the first half roller for all flow conditions

5. CONCLUSIONS

New experiments were conducted in hydraulic jumps using dual-tip phase-detection probes to characterise the air-water turbulent flow properties. The air-water interfacial velocity, turbulence intensity, advection length scale and integral turbulent length and time scales were deduced from a statistical analysis of the probe signal. The turbulent length and time scales were seen quantitatively comparable in the longitudinal and transverse directions, highlighting the existence of transverse flow structures in the hydraulic jump roller, despite the pseudo-two-dimensional flow pattern.

High total turbulence levels were recorded in the roller free-surface region linked to the existence of self-sustained instabilities. The hydrodynamic instabilities took place in the form of pseudo-periodic free-surface deformations and large-scale turbulent flow structures. Their characteristic frequencies were between 0.4 and 4 Hz. The influence of both low-frequency motion and high-frequency turbulence was quantified using a triple decomposition technique applied to the raw air-water detection signal. The frequency thresholds were set at 0.33 Hz and 10 Hz. The signal decomposition showed a significant reduction in turbulence intensity and characteristic turbulent scales for the high-frequency signal component. The velocity fluctuation data showed a large energy component in the slow fluctuation range, and the 'true' (high-frequency) turbulent motion components were smaller than the total. The 'true' turbulence intensity Tu" was shown between 0.5 and 1.5 close to the jump toe and it decreased with increasing distance from the jump toe. The magnitude in 'true' turbulence levels was comparable to earlier studies in absence of large fluctuating motion. The high-frequency advection length scale and integral turbulent length scale exhibited some maxima in the lower shear flow next to the invert. The turbulent length scales decreased along the roller as the fast turbulence was dissipated. Comparison between the longitudinal advection and integral length scales indicated that the advection and diffusion were not independent processes in the flow region immediately downstream of the toe. The impact of slow fluctuations was large in the free-surface region and relatively smaller in the lower shear flow.

The present study provided an important measure of turbulent scales in hydraulic jumps with consideration of bubble-turbulence interaction. It further demonstrated a successful application of the triple decomposition technique to the hydraulic jump flow. The results successfully quantified the turbulence that was truly related to the random fast velocity fluctuations, hence highly improved the quality of turbulence characterisation.

ACKNOWLEDGMENTS

The authors thank Dr Stefan Felder (The University of New South Wales) for his software development that facilitated the triple decomposition calculations. They thank Jason Van Der Gevel (The University of Queensland) for manufacturing the phase-detection probes. The financial support of the Australian Research Council (Grant DP120100481) is acknowledged.

REFERENCES

Chachereau, Y., and Chanson, H. (2011). Free-surface fluctuations and turbulence in hydraulic jumps. *Experimental Thermal and Fluid Science,* 35 (6), 896–909. doi:10.1016/j.expthermflusci.2011.01.009

Chanson, H. (1995). Air entrainment in two-dimensional turbulent shear flows with partially developed inflow conditions. *International Journal of Multiphase Flow*, 21 (6), 1107-1121.

Chanson, H. (2006). *Air bubble entrainment in hydraulic jumps – Similitude and scale effects*. Academic Report No. CH57/05, Dept. of Civil Engineering, The University of Queensland, Brisbane, Australia.

Chanson, H. (2010). Convective transport of air bubbles in strong hydraulic jumps. *International Journal of Multiphase Flow*, 36 (10), 798-814. doi:10.1016/j.ijmultiphaseflow.2010.05.006

Chanson, H., and Carosi, G. (2007). Turbulent time and length scale measurements in high-velocity open channel flows. *Experiments in Fluids,* 42 (3), 385-401. doi:10.1007/s00348-006-0246-2

Chanson, H., and Toombes, L. (2002). Air-water flows down stepped chutes: turbulence and flow structure observations. *International Journal of Multiphase Flow*, 28 (11), 1737-1761.
Cox, D., and Shin, S. (2003). Laboratory measurements of void fraction and turbulence in the bore region of surf zone waves. *Journal of Engineering Mechanics,* 129, 1197-1205.
Felder, S. (2013). *Air-water flow properties on stepped spillways for embankment dams: aeration, energy dissipation and turbulence on uniform, non-uniform and pooled stepped chutes.* PhD thesis, School of Civil Engineering, The University of Queensland, Brisbane, Australia.
Felder, S., and Chanson, H. (2014). Triple decomposition technique in air–water flows: application to instationary flows on a stepped spillway. *International Journal of Multiphase Flow*, 58, 139-153. doi:10.1016/j.ijmultiphaseflow.2013.09.006
Hoyt, JW., and Sellin, RHJ. (1989) Hydraulic Jump as 'Mixing Layer'. *Journal of Hydraulic Engineering*, ASCE, 115(12), 1607-1614
Leandro, J., Carvalho, R., Chachereau, Y., and Chanson, H. (2012). Estimating void fraction in a hydraulic jump by measurements of pixel intensity. *Experiments in Fluids*, 52 (5), 1307-1318.
Lennon, JM., and Hill, DF. (2006). Particle image velocity measurements of undular and hydraulic jumps. *Journal of Hydraulic Engineering*, ASCE, 132 (12), 1283-1294.
Leutheusser, HJ., and Kartha, VC. (1972). Effects of Inflow Condition on Hydraulic Jump. *Journal of Hydraulic Division*, ASCE, 98 (HY8), 1367-1385.
Liu, M., Rajaratnam, N., and Zhu, D. (2004). Turbulence structure of hydraulic jumps of low Froude numbers. *Journal of Hydraulic Engineering*, 130 (6), 511–520. doi:10.1061/(ASCE)0733-9429(2004)130:6(511)
Long, D., Rajaratnam, N., Steffler, PM., and Smy, PR. (1991). Structure of flow in hydraulic jumps. *Journal of Hydraulic Research*, IAHR, 29 (2), 207-218.
Longo, S. (2011) Experiments on turbulence beneath a free surface in a stationary field generated by a Crump weir: turbulence structure and correlation with the free surface. *Experiments in Fluids*, 50, 201-215.
Lubin, P., and Glockner, S. (2013). Detailed numerical investigation of the three-dimensional flow structures under breaking waves. *7th Conference on Coastal Dynamics*, Arcachon, France, 1127-1136.
Mignot, E., and Cienfuegos, R. (2010). Energy dissipation and turbulent production in weak hydraulic jumps. *Journal of Hydraulic Engineering*, ASCE, 136 (2), 116-121.
Mossa, M. (1999). On the oscillating characteristics of hydraulic jumps. *Journal of Hydraulic Research,* IAHR, 37 (4), 541-558.
Mossa, M., and Tolve, U. (1998). Flow visualization in bubbly two-phase hydraulic jump. *Journal of Fluids Engineering*, ASME, 120, 160-165.
Mouaze, D., Murzyn, F., and Chaplin, JR. (2005). Free surface length scale estimation in hydraulic jumps. *Journal of Fluids Engineering*, Transactions ASME, 127, 1191-1193. doi:10.1115/1.2060736
Murzyn, F., Mouaze, D., and Chaplin, JR. (2007). Air-water interface dynamic and free surface features in hydraulic jumps. *Journal of Hydraulic Research*, IAHR, 45 (5), 679-685.
Murzyn, F., and Chanson, H. (2009). Experimental investigation of bubbly flow and turbulence in hydraulic jumps. *Environmental Fluid Mechanics*, 9 (2), 143-159. doi:10.1016/j.expthermflusci.2009.06.003
Peregrine, DH., and Svendsen, IA. (1978). Spilling breakers, bores and hydraulic jumps. *Proc. 16th International Conference on Coastal Engineering*, Hamburg, Germany.
Prosperetti, A., and Tryggvason, G. (2009). *Computational methods for multiphase flow*. Cambridge University Press, London, UK.
Rajaratnam, N. (1962). An experimental study of air entrainment characteristics of the hydraulic jump. *Journal of Instruction Engineering India,* 42 (7), 247-273.
Resch, FJ., and Leutheusser, HJ. (1972). Le ressaut hydraulique: mesure de turbulence dans la région diphasique. *Journal La Houille Blanche*, 4, 279-293 (in French).
Richard GL (2013) *Élaboration d'un modèle d'écoulements turbulents en faible profondeur: application au ressaut hydraulique et aux trains de rouleaux*. PhD thesis, Institut Universitaire des Systèmes Thermiques Industriels, Univerité d'Aix-Marseille, Marseille, France (in French).
Richard, GL., and Gavrilyuk, SL. (2013). The classical hydraulic jump in a model of shear shallow-water flows. *Journal of Fluid Mechanics*, 725, 492-521. doi:10.1017/jfm.2013.174
Svendsen, IA., Veeramony, J., Bakunin, J., and Kirby, JT. (2000). The flow in weak turbulent hydraulic jumps. *Journal of Fluid Mechanics*, 418, 25-57.
Wang, H., and Chanson, H. (2014). Air entrainment and turbulent fluctuations in hydraulic jumps. *Urban Water Journal*. doi:10.1080/1573062X.2013.847464
Wang, H., Felder, S., and Chanson, H. (2014). An experimental study of turbulent two-phase flow in hydraulic jumps and application of a triple decomposition technique. *Experiments in Fluids*, 55 (7), 1-18. doi:10.1007/s00348-014-1775-8
Zhang, G., Wang, H., and Chanson, H. (2013). Turbulence and aeration in hydraulic jumps: free-surface fluctuation and integral turbulent scale measurements. *Environmental Fluid Mechanics*, 13 (2), 189–204. doi:10.1007/s10652-012-9254-3

